Article

Journal of Advanced Electrochemical Storage

www.pubj.org

Impact of Chromium doped on the Magnetic and Structural Properties of Barium Ferrite ($BaFe_{12-x}Cr_xO_{19}$) synthesized by Co-precipitation Method

S. Vadivelan[1]*, S. Sowmiya[1]

1,*Department of physics, Karpaga Vinayaga College of Engineering and Technology, Chengalpattu - 603305, Tamil Nadu, India.

1, Department of physics, SRM Valliammai Engineering College, Kattankulathur, 603203, Tamil Nadu, India.

Cite This: *J. Adv. Electro. Storage* 2026, 1, 73−85.

ABSTRACT: Barium ferrite is commonly utilized due to its exceptional characteristics as a magnetic recording material with high density. The co-precipitation process will be used in this study to produce the chromium doped barium ferrite at various ratios. This is done to increase the material's permeability and prevent magnetic loss. Samples of chromium-doped barium ferrite in varying ratios (1–5 %) are subjected to a 6-hour sintering process at 1000°C, followed by an X-ray powder diffraction study. According to the analysis, the measured values are in agreement with the conventional parameters (a=b=5.864 Å and c=23.099 Å), confirming that the samples are part of the hexagonal system. X-ray beams are used to evaluate the sample's binding energy and obtain XPS spectra. Magnetic saturation, magnetic remanance and coercivity are measured by the vibrating sample magnetometer (VSM). From UV analysis, the measured band gap value for pure barium ferrite is 2.944 eV.

Keywords: Magnetic materials, saturation magnetization, coercivity, ferrites.

1. INTRODUCTION

A substance with a high packing density and potent magnetic characteristics is barium ferrite. Because of its magnetic properties and resistance to oxidation, corrosion, and temperature, it is frequently used in magnetic tapes, speakers, and card strips. Exploration of barium ferrite for long-term data storage systems has been the focus of recent developments [1-2]. Additionally, the material has demonstrated resistance to a variety of environmental stressors, such as corrosion and dampness. It is impossible to further oxidize ferrites because they are already oxidized. This is one of the factors that contribute to ferrites' exceptional resistance to corrosion and heat demagnetization. They become more resilient to thermal demagnetization as the temperature of barium ferrite increases due to the enhancement of their high intrinsic coercivity [3-4]. In this characteristic of barium ferrite loudspeaker, motor and generator designs applications.

Researchers are very interested in synthesizing the manganese cobalt oxide material via common methods including sol-gel, combustion technique, ball milling, solid-state reaction, solvothermal, mechanochemical method, hydrothermal and wet chemical. However, some of these methods are frequently used and costly, unreliable, and challenging for large-scale production. Among them, chemical techniques, co-precipitation is cost-effective and the best method due to it providing homogeneous size distribution, required surface morphology and purity.

Because ferrite magnets are such excellent insulators, no electrical current can pass through

them. They are also brittle, which is a feature of ceramics. Additionally, ferrite magnets have outstanding machining qualities that enable the material to be machined into a wide variety of forms and sizes. Although barium ferrites have been used to store data on tapes and magnetic strips because they are generally stable to moisture and resistant to corrosion, their utility for high capacity data storage has reached its limit. As the size of the barium ferrite particles decreases, a thicker passivation coating is required to stop oxidation and deterioration. Due to the fact that it is already oxidized, barium ferrite totally outclasses metal particles. Therefore, a protective layer cannot limit its size. Barium ferrite's hexagonal pattern makes it easier to organize than the disorganized rod-like metal particles [5-7].

Globally, the material is used in permanent magnets, magnetic stripe cards (like credit cards, hotel keys, and ID cards), and recording devices like tapes and other media devices. Because of its stability, the material can be significantly reduced in size, which results in a much higher packing density. The oxide has lately been replaced by barium ferrite, which has substantially higher coercivity levels. This makes the material magnetically hard, which makes it more suitable for barium ferrite. The tiny reader that is implanted with the magnetic barium ferrite pattern allows the scanner to identify the card because it identifies the pattern that is also included in the barcode [8-10]. Through a process known as sintering, in which powdered barium ferrite is forced into a mold and heated until it fuses together, the materials may be shaped into nearly any size and shape. The barium ferrite retains its magnetic characteristics even after solidifying into a block. The magnets have been used in speaker units for a long time because of their exceptional resistance to demagnetization.

Because of its high packing density, barium ferrite has been identified as a special storage medium for Linear Tape-Open (LTO) storage and is crucial in determining the direction of LTO tapes in the future [11-13]. The recording area rises in proportion to the increase in packing density. This contrasts sharply with metal particle technology, which has begun to wane because to issues with particle shrinkage beyond 100 nm. Because of its higher packing density and hexagonal shape, barium ferrite can be stacked much more effectively and reduced to significantly smaller sizes. Increasing the coercivity of barium ferrite is the goal of adding divalent cations like chromium. The aforementioned claim is validated by the (VSM) magnetic characterization.

This work's main goal was to improve the storage capacity by determining the influence of certain amalgamation factors on the magnetic properties of barium ferrite made using the co-precipitation procedure. The fact that this homogenous reaction produces fine particles is a crucial aspect of this technique. Excellent reactivity powder was created from the reaction to coincide with the drop in sintering temperature [14-17]. In contrast to alternative methods of preparation, the co-precipitation process yields outcomes that are highly precise, lucid, and economical.

2. EXPERIMENTAL

2.1. Materials

The co-precipitation process was used to create the chromium-doped and undoped barium ferrite powder materials. Ammonium hydroxide (NH_4OH), citric acid ($C_6H_8O_7$), ferric nitrate (Fe $(NO_3)_3$), chromium nitrate (Cr (NO3)2), and purified barium nitrate (Ba $(NO_3)_2$) were all acquired from scientific material and technology.

Ammonium hydroxide (NH_4OH) was combined with distilled water, citric acid (C6H8O7), and the stoichiometric quantities of barium nitrate (Ba $(NO_3))_2$, ferric nitrate (Fe (NO3)3), and chromium nitrate ((Cr $(NO3)_2$). The clear product is obtained by using citric acid. Ammonium hydroxide completely controls the

synthesis process, which yields different chromium nitrate doping percentages using the co-precipitation method. Filtration was used to collect the precipitated materials, which were then washed away four times using distilled water. The final precipitate material is dried for six hours at 80°C. After drying, the material is ground into a powder and heated to 1000°C for six hours to undergo the sintering process. Lastly, this method yields the composition of chromium doped barium ferrite ($BaCr_xFe_{12-x}O_{19}$).

2.3. Materials characterization

Using CuKα radiation (λ = 1.541 Å) in the 10° to 80° range, Bruker D2 Phaser Powder X-ray diffractometry is used to determine the crystal structure of the produced ferrite powders. Using a Netzsch STA 409, thermo gravimetric analysis and differential thermal analysis are carried out on the sample materials at a rate of 20°C per minute over a temperature range of 20–1000°C. Opus 6.5 (version) software is used by the FTIR Spectrophotometer of BRUKER ALPHA to examine the formation of pure and doped chromium ferrite. Using a Kratos Analytical Axis Ultra DLD with an aluminium anode as the source and running at 160 eV pass energy, the oxidation states of these samples were determined by X-Ray Photoelectron Spectroscopy (XPS). The VEGA3 TESCAN scanning electron microscope (SEM) was used to examine the samples' morphology.

The vibrating sample magnetometer (VSM) Lakeshore (7410) which is used to characterized the magnetic properties of the sample at room temperature with the help of applied magnetic field (20 kOe). The materials are characterized using models of UV-visible spectrophotometers, such as the Thermo Scientific GENESYS 30.

3. RESULTS AND DISCUSSION

3.1. Differential Thermal Analysis (DTA) / Thermo gravimetric Analysis (TGA)

This examination is used to identify the properties of materials that show either mass gain or loss as a result of oxidation and decomposition. The degradation mechanisms, reaction kinetics, organic content, and inorganic (such as ash) content of a sample are all examined using TG/DTA [18]. Thermo gravimetric / differential thermal analysis represents an indispensable methodology for scrutinizing the thermal stability and creation of barium ferrite nanoparticles. The composition of the precursor materials and the particular TG/DTA curves in conjunction with their interpretation are contingent upon the synthesis technique that is employed.

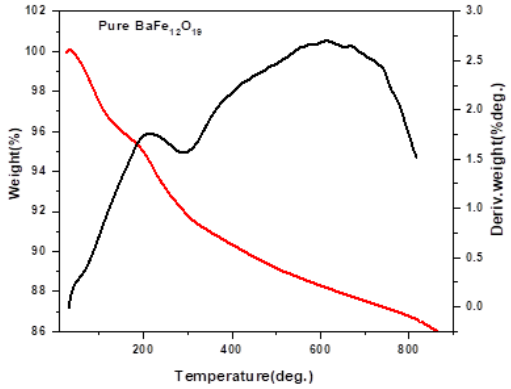

Fig. 1 DTA/ TGA pattern for pure barium ferrite

The TG/DTA examination of barium ferrite precursors typically exhibits several phases of diminished weight and corresponding thermal occurrences as the substance undergoes heating. Low-temperature occurrences approximately 50–200 °C. A slight initial diminishing of weight can be seen in the TGA curve, and corresponding to the diminished weight in the DTA curve, there is a wide, shallow endothermic peak. This phase is brought about by the vaporization of moisture that has been physically absorbed, solvents like ethanol or water, and additional volatile constituents present on the surface and inside the precursor powder's pores. The temperature 200–600 °C (TGA) a major, more substantial diminished

weight takes place within this spectrum, and concurrently, the diminished weight corresponds to a sequence of exothermic peaks that are evident within DTA [19-20]. This region signifies the breaking down of the precursor's organic components, particularly within the co-precipitation method; this entails the disintegration of organic fuels such as glycine or citric acid, as well as metal nitrates.

The combustion of these organic substances results in the release of heat, which is represented by the exothermic peaks. The Intermediate phase decomposition like 600–800 °C, a gradual diminished weight (TGA) persists within this spectrum, and the manifestation of a broad exothermic occurrence is possible, hinging on the intermediate reactions (DTA). The disintegration of any residual or intermediate compounds, such as barium carbonate ($BaCO_3$) and other iron oxides like hematite (Fe_2O_3), is linked to this stage as they interact to generate the definitive ferrite phase. Finally 800-1000°C the phase of barium ferrite is shaped. In this section, the diminished weight reaches stability, and the curve transitions into a comparatively level state (TGA), with observable distinct exothermic peaks (DTA). The steadiness of the TG curve implies the elimination of all volatile constituents and the high-temperature solid-state reaction that produces crystalline barium ferrite. The shift of intermediate phases into the desired hexagonal barium ferrite structure is indicated by the exothermic peaks. The temperature at which this definitive exothermic peak transpires ascertains the minimum calcination temperature that is requisite for yielding a product that is well-crystallized [21-22].

A multi-step diminishing of weight can be observed, accompanied by exothermic peaks that materialize at precise temperatures. In the case of a precursor encompassing barium and iron oxalates, exothermic peaks manifest around 45, 220, 416, and 615 °C, thereby signifying sequential phases of decomposition. This examination enables researchers to ascertain the suitable temperature for calcination, guaranteeing the exhaustive combustion of organic substances and the crystallization of the nanoparticles.

3.2. X-Ray Diffraction Analysis

The X-ray diffraction patterns acquired for both the BaFe12O19 compounds, in their pure state and when laced with chromium, are presented in Fig. 2. The distinct peaks observed in the XRD patterns validate the hexagonal crystal structure, aligning perfectly with the JCPDS reference 78-0133. Pronounced diffraction peaks from the pure and chromium-integrated $BaFe_{12}O_{19}$ samples distinctly showcase typical peaks at 2θ values that correlate with the (110), (107), and (114) planes, respectively [23]. In the XRD pattern, the absence of any peaks other than those of $BaFe_{12}O_{19}$ implies the high purity of the synthesized samples. Peak broadening suggests an increased surface-to-volume ratio coupled with a reduction in particle diameter.

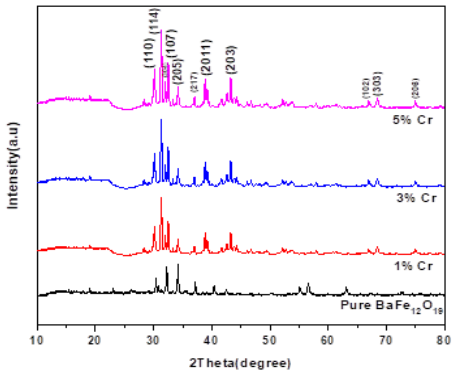

Fig. 3 XRD pattern of the samples: (a) Pure nanobarium ferrite and (b) Cr-1mol %, (c) Cr-3mol %, (d) Cr-5mol % doped nanobarium ferrite.

The mean crystallite dimensions (t) of the synthesized ferrite samples were ascertained using the Scherrer formula.

$$t=k\lambda / (\beta \cos\theta) \quad (1)$$

Here, k symbolizes the Scherrer constant (k=0.89), λ stands for the X-ray radiation's wavelength (λ=1.54 Å), β represents the diffraction peak's full width at half maximum, and θ signifies the diffraction angle [24-26]. The crystallite size (t) of the investigated samples, derived directly from a single-line assessment of the XRD reflections, is shown in Table 1. The data reveals that pure barium ferrite has a crystallite size of 49.366 nm; however, this size decreases with the incorporation of varying Cr2+ doping levels in the barium ferrite.

Consequently, it's inferable that crystallite size is heavily influenced by Cr2+ concentration, which hinders grain development, leading to a decline in crystallite size as its concentration rises [27-29]. According to Table 1, the elastic strain value sees an increase with a corresponding increase in Cr2+ concentration. This implies a scenario where chromium ferrite particles potentially grow with more significant defects in the favored direction, transitioning towards a diminished crystallite size. The lattice constant (a) is ascertained for all compositions using this formula,

$$1/d^2 = 4/3 [(h^2+hk+k^2)/a^2] + l^2/c^2 \quad 2)$$

where d represents the d-spacing value of a line in the XRD pattern, and (hkl) denotes the Miller indices. Table 1 provides a listing of the calculated lattice constant values for all the samples prepared, with an accuracy of ±0.003 Å. The data in the table indicates that the lattice constant (a) becomes larger with an elevated Cr2+ concentration, which also increases the specific surface area of the particles. The elastic strains present in the samples are also quantified using the ensuing expression [30-32],

$$\varepsilon= \beta/(2\cot(\theta)) \quad (3)$$

The elastic constant values are indexed in Table 1. As the Cr2+ concentration rises, there's a corresponding increase in the samples' elastic constant value.

Using the Williamson and Hall method, the average crystallite size and strain introduced by the doped Cr2+ concentration were calculated with the expression shown below [33],

$$\beta\ (hkl)\ \cos\theta\ (hkl) = K\lambda/D + 4\varepsilon\sin\theta(hkl) \quad (4)$$

Here, K is a constant (0.89), λ is the wavelength of CuKα (1.5406 A°), D denotes the crystallite size in nanometers, β stands for the full width at half maximum (FWHM) of XRD peak intensity, h is the peak position (Bragg angle), and ε represents the micro strain. The plot of Williamson–Hall is constructed using β (hkl) Cosθ and 4sinθ (hkl), where the slope of the line is indicative of the strain, as displayed in Fig. 3.

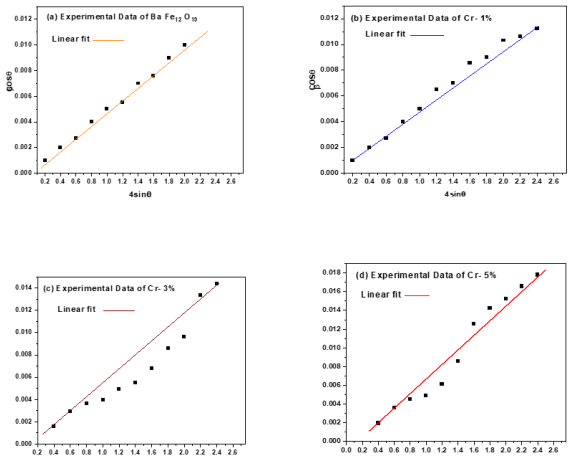

Fig. 3. Williamson–Hall plot of the powder samples: (a) Pure barium ferrite, (b) Cr-1 mol%, (c) Cr-3 mol% and (d) Cr-5 mol% doped barium ferrite.

Table 1 Summary of Pure and Cr- doped nano barium ferrite Calcined at 1000 ^{o} C

Composition / 1000^{o} C	Crystalline size (nm)	Average crystallin e size	a (Å)	c (Å)	Elastic Strain

	Scherrer method	W-H method	't'(nm)			ε (X 10-3)
Pure	48.316	50.416	49.366	5.865	23.099	3.435
1mole % Cr	49.326	51.626	50.476	5.868	23.102	2.819
3 mole % Cr	49.422	51.822	50.622	5.868	23.102	2.691
5 mole % Cr	49.438	51.938	50.688	5.871	23.105	2.671

3.3. Fourier Transforms Infrared Spectroscopy Analysis (FT-IR)

The investigation of chemical bonding within a compound has been achieved through the utilization of FTIR spectrum analysis. The specific configuration of the crystal structure, morphology, and chemical makeup of the materials exert a distinct influence on the absorption peaks, thereby dictating the character of chemical bonding in both pure and chromium-enhanced barium ferrite compounds [34-35]. Displayed in Fig. 4 is the recorded.

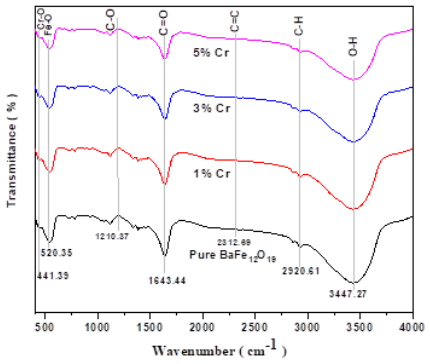

Fig. 4. FT-IR pattern of the samples: (a) Pure nanobarium ferrite, (b) Cr-1mol %, (c) Cr-3mol % and (d) Cr-5mol % doped nanobarium ferrite.

FT-IR spectra of barium ferrite, captured across a spectrum ranging from 400 to 4000 cm−1 wave numbers. These spectral segments commonly serve as identifiers for additional functional groupings or constituents existing within the sample, encompassing water or other molecules that have been adsorbed, with the band situated around 3200-3500 cm-1 frequently linked to the O-H stretching vibrations stemming from adsorbed water or hydroxyl functional groups. The prominent absorption band, observable within the frequency band spanning 400–1000 cm-1, distinctly defines the deformation modalities of Cr–O and Fe–O.

Furthermore, the absorption band surpassing 500 cm−1 arises from the deformation occurring in Fe–O bonds during the distortion of Fe–O–Fe bridges [36-37]. The notable absorption peak, approximately at 1643. 44 Cm^{-1} is correlated with the C=O vibrational mode. Additionally, the absorption band situated within the 3200–3500 cm−1 range is indicative of the OH stretching vibration of water molecules that have been absorbed onto the exterior of the samples, with the absorption peak located around 3447. 27 cm^{-1} [38]. The atmospheric conditional absorption of C=C on the surface of the fabricated samples was discerned from the acute peak found at approximately 2312. 69 cm−1. Based on the spectra, the C–O stretching band at 1210. 37 cm^{-1} is recognized as a consequence of elevated concentrations of doped chromium nitrate [39]. Thus, the detection of metal oxide vibrations across the frequency span of 400–4000 cm−1 underscores the material phase and chemical integrity exhibited by all the pure and Cr^{2+}-doped $BaFe_{12}O_{19}$ compounds.

3.4. X-Ray photoelectron spectroscopy studies (XPS)

The examination of chemical states and surface characteristics of the synthesized sample was performed via X-Ray photoelectron spectroscopy (XPS). The comprehensive XPS spectrum of chromium-doped barium ferrite produced through the co-precipitation method is depicted in Fig. 5. Within this spectrum, the photoelectron peaks corresponding to Cr 2p, Fe 2p, and O 1s, alongside C 1s, were detected [40].

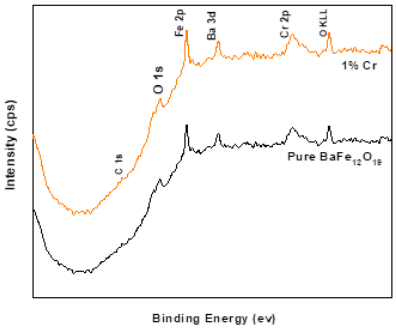

Fig. 5. XPS spectrum: (a) pure nanobarium ferrite and (b) Cr-1mol % doped nanobarium ferrite.

As shown in Fig. 6 (b), the Ba 3d5/2 and Ba 3d3/2 peaks are evident at 534.52 and 519.71 eV, respectively, and are employed for characterizing the sample. The data suggests a minor variation in the binding energy of the Ba peak in the ferrite substance relative to that in BaO, largely attributable to the differing settings of the Ba2+ ion within the compounds. Fig. 6a presents the XPS bands of the cr-doped ferrite, revealing peaks for Cr 2p3/2 and Cr 2p1/2 at binding energy values of 540.73 eV and 537.47 eV, in that order. These peaks substantiate the presence of the Cr2+ ion in the chromium ferrite particles [41- 43]. Fig. 6c portrays the Fe 2p core shell XPS spectra of chromium ferrite. This outcome closely matches prior findings in scholarly sources for the Fe3+ ion found in ferrite materials. Notably, the high-resolution XPS spectra of Fe 2p, as illustrated in Fig. 6c, can be resolved into a pair of separate peaks situated at 544.63 eV and 515.28 eV. The energies at which binding occurs align with the binding energies observed in Fe 2p3/2-Fe2+ and Fe 2p3/2-Fe3+ ions. As a result, the iron (Fe) within the synthesized nanoparticles undeniably features a combination of Fe3+ and Fe^{2+} ions, as evidenced in prior research [44-46]. The examination of the O 1s region using XPS spectra revealed a peak at 468.82 eV, detailed in Fig. 6d. This particular peak is linked to the energy of O2- metal groupings detected on the material's surface.

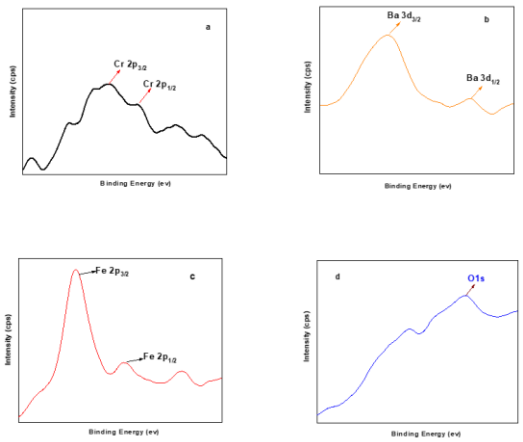

Fig. 6 XPS high resolution spectrum: (a) Cr 2p, (b) Ba 3d, (c) Fe 2p and (d) O 1s

3.5. Scanning Electron microscope (SEM)

Figure 7 shows the SEM picture of pure nanobarium ferrite that was created using a chemical co-precipitation method at a sintering temperature of 1000°C. From the scanning electron microscopy investigation, the grain size and morphology of the prepared pure and chromium-doped barium ferrite samples are found. As the proportion of Cr doped increased, the grain size grew (Fig. 7).

According to Fig. 7, as the proportion of chromium doped increases from 0 to 5%, the grain size increases by 500 nm to 1 µm. The air gap between the barium ferrite particles is relatively high, which weakens the bonds between the separated particles. The primary

purpose of this characterisation is to determine the material's porosity.

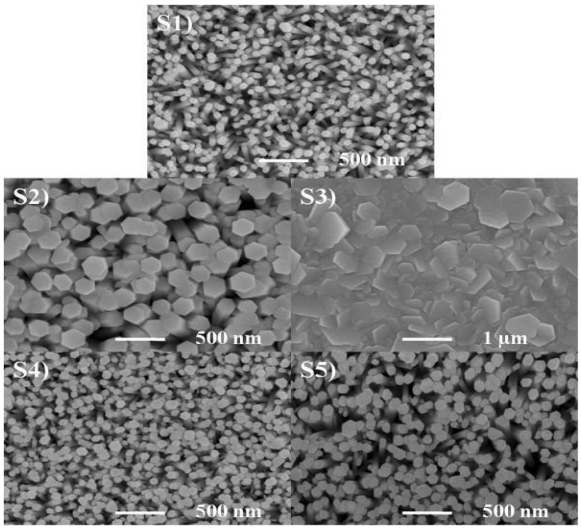

Fig. 7 SEM image of the Pure nanobarium ferrite.

From the SEM image that the grains are non-uniform and densely distributed on the surface, more over the grain size of the ferrite found to be in the range of 1µm -500nm [47-49].

3.6. Vibrating Sample Magnetometer analysis (VSM)

The vibrating sample magnetometer measures the magnetic saturation and coercivity value of a sample of magnetic material is placed in an external magnetic field by converting the dipole field of the sample into an ac electrical signal.

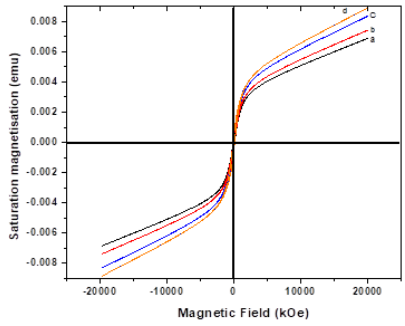

Fig. 7 Hysteresis pattern for the samples: (a) Pure nanobarium ferrite and (b) Cr-1mol%, (c) Cr-3mol % and (d) Cr-5mol % doped nanobarium ferrite.

From the analysis, the pure and Cr2+ doped(x= 1%, 3% and 5%) barium ferrite hysteresis loops are shown in Fig. 8. The magnetic measurements of the data are summarized in Table 2. After doping, the observed saturation magnetization (Ms) increases from 68.04 to 88.48 emu/g with increase in the chromium percentage [50-51]. The saturation magnetization (Ms) value of pure barium ferrite is 68.04 emu/g at 300K. From the hysteresis loop, the remnant magnetization (Mr) of the pure and Cr2+ doped barium ferrite are increases with increase in doped percentage of Cr2+. The remnant magnetization (Mr) at 300K for pure and Cr2+ (1%) doped barium ferrite is 2.11 emu /g and 2.32 emu /g -5.37 emu /g. The squareness (SQR) value of these samples is calculated by this ratio (Mr/ Ms). In general, large SQR values are favored in many magnetic storage applications. The SQR value increases with increasing doped percentage of Cr2+ [52-54]. The SQR value of the pure barium ferrite sample at 300 K is 0.031 and doped percentage of Cr2+ increased thereby increasing the SQR value simultaneously.

Table 2 Summary of pure and Cr- doped nanobarium ferrite calcined at 1000 ^{o} C

Composition / 1000° C	Ms (Saturation magnetization) (emu/g)	Mr (Remnant magnetization) (emu/g)	(Mr/Ms) ratio	Hc (Coercivity) (Oe)
Pure	68.04	2.11	0.031	287
1mol%Cr	73.64	2.32	0.032	289
3 mol%Cr	82.28	4.95	0.060	423
5 mol%Cr	88.48	5.37	0.061	428

From the hysteresis loop, the SQR value of 5% chromium doping is calculated as 0.061 at 300 K. However, the SQR values depend on the doping percentage of Cr2+. The coercivity value for pure barium ferrite is 2.87 Oe at 300K. In addition the chromium doping percentage (1-5%) increased with varying the coercivity values (2.87

Oe – 4.28 Oe). After doping, the observed Ms value decreases from 68.04emu/g to 88.48emu/g with increase in the Cr2+ doped percentage [55]. From the data, SQR value is obtained as dependency of the Cr2+ doped percentage. SQR and coercivity value is varied from the prepared sample density.

3.7. UV–Visible spectroscopic analysis and direct energy band gap calculation of barium ferrite nanoparticles (UV)

Fig. 8 shows UV-visible investigations performed on samples of pure barium ferrite to analyze their absorption. Another somewhat simple and inexpensive characterisation technique that is frequently employed for the investigation of nanoscale materials is UV-visible spectroscopy. It calculates how much light is reflected or absorbed from a sample and contrasts that amount with that of a reference material. UV-Vis spectroscopy is a crucial method for identifying, characterizing, and studying nanomaterials since their optical characteristics are sensitive to factors like size, shape, concentration, aggregation state, and refractive index close to the nanoparticle surface [56-57]. Figure 8 displayed the UV-visible absorption spectra of BFO nanoparticles in the 200–700 nm wavelength range. A noticeable absorption band can be seen in the spectra, peaking at 251, 282, 325, and 593 nm.

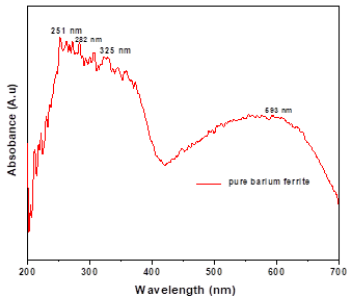

Fig. 8 UV visible spectra for pure barium ferrite

These peaks represent an electrical transition in which a valence band electron absorbs energy from incident UV light and is stimulated to a higher energy level, possibly in the conduction band. This could entail transitions between localized pure barium ferrite energy levels and the host lattice's wider energy bands. This phenomenon is triggered by the Ba-O-Fe bonds' metal oxygen vibrations. Due to the quantum effect, the shift may be attributed. Using this relation, the band gap value has been calculated for pure barium ferrite.

$$E = hc/\lambda \text{ ev} \quad \ldots\ldots\ldots\ldots\ldots \quad (5)$$

From the figure 8, measured band gap value for pure barium ferrite is 2.944 eV. The Fe3+ ion exhibited a sextet state and a 3d5 configuration in the hexagonal crystal area. In the meanwhile, parity and spin symmetry were prohibited for these transitions. This led to the prediction of very weak crystal field transitions. Additionally, a high absorption at 251 nm is typically linked to the charge transfer transition from O2− to Fe3+ (Xie et al., 2013). While the less intense absorption band at 282 nm corresponds to the charge transfer transition from O2- to Fe3+, the strong absorption band at 325 nm may be caused by an electron moving from the valence band to the conduction band in the host lattice [58-62]. Additionally, transitions involving extrinsic states, such as surface states or impurities, were expected to cause the 380 nm absorption band. Co-precipitation-synthesised nanoparticles typically have a high surface-to-volume ratio. The absorbance spectra of pure barium ferrite in transmission mode were obtained by uniformly dispersing the particles in liquid paraffin, in the wavelength range of 200–700 nm, in order to estimate the band gap in the nanomaterials.

4. CONCLUSION

Barium ferrite with chromium doping, exhibiting a hexagonal configuration, was successfully produced using a method involving simultaneous precipitation. According to the XRD analysis, the presence of pure barium ferrite and 1%, 3%, and 5% Cr2+ infused barium ferrite

verifies a hexagonal arrangement. The SEM pictures illustrate that the particle sizes of the pure barium ferrite sample range from 1 µm to 500 nm. The magnetization studies indicate that the saturation magnetization (Ms) value decreases when the percentage of Cr2+ infused barium ferrite increases from 0-5%, going from 68.04 emu/g to 88.48 emu/g; similarly, the remnant magnetization (Mr) diminishes from 2.11 emu/g to 5.37 emu/g with the same increase of 0-5% of Cr2+ doped barium ferrite. The coercivity (Hc) experiences a reduction from 287 Oe to 428 Oe as the proportion of Cr2+ doping is elevated from 0% to 5% at a temperature of 300K. It was found that the magnetic behaviour is strongly influenced by temperature changes. The magnetic characteristics of the samples are noticeably impacted during the preparation and sintering stages. The UV-visible absorption spectra of pure barium ferrite nanoparticles in the 200–700 nm wavelength range. A noticeable absorption band can be seen in the spectra, peaking at 251, 282, 325, and 593 nm and band gap value for pure barium ferrite is 2.944 eV. The central objective of this study is to expand how much this substance can hold, since we can bypass having lots of storage capacitors, which is easier. The way these samples act magnetically changes a lot depending on how they are made and how they are heated. This approach is quite simple, doesn't cost much, and the space needed to prepare it works well. Looking at what we found and how we tested it, this approach stands out when you compare it to other approaches.

Author contributions

S. Vadivelan: Writing-original draft, Conceptualization, Writing-review and editing, Methodology, Investigation; S. **Sowmiya:** Writing-review and editing, Formal analysis, Methodology.

Conflicts of interest

There are no conflicts to declare.

References

[1] Sozeri, H. Kucuk, L. Ozkan, H. Improvement in magnetic properties of La substituted BaFe12O19 particles prepared with an unusually low Fe/Ba molar ratio, Journal of Magnetism and Magnetic Materials 323 (2011) 1799-1804.

[2] Salvi, S.V. Joshi, V.H. Effect of PH on magnetic properties of doped barium hexaferrite, Indian Journal of Pure & Applied Physics 4 (2009) 277-281.

[3] Gubin, S.P. Koksharov Yu, A. Khomutov, G.B. Yurkov Yu,G. Magnetic nanoparticles: preparation, structure and properties, Russian Chemical review 74 (2005) 489-520.

[4] Murthy, Y.L.N. Kasiviswanath, I.V. Synthesis and characterization of nickel copper ferrite, International Journal of ChemTech Research 1 (2009) 1308-1314.

[5] Arumugam Raja, Ro Mu Jauhar, Kasthuri Ramachandran, Sivasubramani Vediyappan, Ramesh Kumar Raji, Muthu Senthil Pandian, Ramasamy Perumalsamy, A Quintuple-Layered Binary Chalcogenide Sb2Te3 Single Crystal and Its Transport Properties for Thermoelectric Applications, ACS omega, 7(32), (2022) 27798-27803.

[6] Hessien, M. Rash ad, M. El-Barawy, K. Controlling the composition and magnetic properties of strontium hexaferrite synthesized by co-precipitation method, J. Magn. Magn. Mater. 320 (2008) 336–343.

[7] Dang, P. Wei, Y. Liu, D. Li, G. Lin, J. Recent advances in chromium-doped near-infrared luminescent materials: fundamentals, optimization strategies, and applications Adv. Opt. Mater., 11 (3) (2023), p. 2201739.

[8] V Govindan, Arumugam Raja, Gour Mohan Das, D Joseph Daniel, R Ramesh Kumar, K Sankaranarayanan, Synthesis

and luminescence properties of Ca3Ga4O9: Eu3+: An efficient red-emitter for WLEDs, Ceramics International, 49 (11), 17566-17576, (2023).

[9] T. Ramachandran, F. Hamed, R.K. Raji, A.H.I. Mourad, Room temperature ferromagnetism in garnet type Dysporisum ferrite by coprecipitation approach, in 2022 Advances in Science and Engineering Technology International Conferences (ASET), Dubai, United Arab Emirates, 2022, pp. 1–5,

[10] Kannan, Y. Saravanan, R. Srinivasan, N. Praveena, K.Sadhana, K. Synthesis and characterization of some ferrite nanoparticles prepared by co-precipitation method J. Mater. Sci.: Mater. Electron. 27 (2016), pp. 12000-12008.

[11] Garcia-Casillas, P.E. Beesley, A.M. Bueno, D. Martinez, C.A. Remanence properties of barium hexaferrite, Journal of Alloys and Compounds 369 (2004) 185-196.

[12] Makled, M.H. Matsui, T. Tsuda, H. Mabuchi, H. El- Mansy, M.K. Infrared Spectroscopy and Thermal Stability Studies of Natural Rubber-Barium Ferrite Composites, Journal of Materials Processing Technology 160 (2005) 229-233.

[13] G. Lal, K. Punia, S.N. Dolia, P. Alvi, S. Dalela, S. Kumar, Rietveld refinement, raman, optical, dielectric, m¨ossbauer and magnetic characterization of superparamagnetic fcc-cafe2o4 nanoparticles, Ceramics Int. 45 (5) (2019).

[14] Dhilip, M., Punitha, J.S., Rameshkumar, R. et al. A novel double perovskite oxide Sm2CoFeO6 phosphor for orange LEDs: structural, magnetic and luminescence properties. Appl. Phys. A 128, 324 (2022).

[15] N. Karthikeyan, R. Ramesh Kumar, G. Jaiganesh, K. Sivakumar, Thermoelectric power factor of La0.9M0.1FeO3 (M = Ca and Ba) system: Structural, band gap and electrical transport evaluations, Physica B: Condensed Matter, 529, 2018, 1-8, 0921-4526,

[16] Singh,P. Babbar, V.k. Razdan, A. Srivastava, S.L. Agrawal, V.K. Goel, T.C. Dielectric constant, magnetic permeability and microwave absorption studies of hot-pressed Ba-Co Ti hexaferrite composites in X-band, J. Mater. Sci. 41 (2006) 7190–7196.

[17] J. Stella Punitha, Ramesh Kumar Raji, Tholkappiyan Ramachandran, K. Saravana Kumar, Muthu Dhilip, Fathalla Hamed, A. Nataraj, Influence of Pr^{3+} substitution on the structural, optical, magnetic, and dielectric properties of Sr2FeTiO6−δ double perovskites, Solid State Sciences, Vol. 160, 2025, 107825.

[18] R. Ramesh Kumar, T. Ramachandran, K. Natarajan, et al., Fraction of rare-earth (Sm/Nd)-lanthanum ferrite-based perovskite ferroelectric and magnetic nanopowders, J. Electron. Mater. 48 (2019) 1694–1703,

[19] Ding, J. Miao, W.F. McCormick, P.G. Street, R. High-coercivity ferrite magnets prepared by mechanical alloying, Journal of Alloys and Compounds 281 (1998) 32-36.

[20] Shams, N. Liu, X. Matsumoto, M. Morisako, A. Microstructure and magnetic properties of commercial barium ferrite powders, Journal of Magnetism and Magnetic Materials 290 (2005) 138-140.

[21] Sulaiman, N. Ghazali, M. Yunas, J. Rajabi, A. Majlis, B. Razali, M. Synthesis and characterization of cafe2o4 nanoparticles via co-precipitation and auto-combustion methods Ceramics Int., 44 (1) (2018), p. 46-50.

[22] Márquez, P. Alburquenque, D.Celis, F. Freire, R.M. Escrig, J. Structural, morphological and magnetic properties of iron oxide thin films obtained by atomic layer deposition as a function of their

thickness J. Magnet. Magnetic Mater.,530 (2021), p. 167914.

[23] Qiu, J. Gu, M. Magnetic nanocomposite thin films of BaFe12O19 and TiO2 prepared by sol–gel method, Applied Surface Science 252 (2005) 888-892.

[24] Temuujin, J. Aoyama, M. Senna, M. Masuko, T. Ando, C. Kishi, H. Synthesis of Y-type hexaferrites via a soft mechanochemical route, J. Solid State Chem. 177 (2004) 3903-3908.

[25] Vadivelan, S. Victorjaya, N. Investigation of Structural, Thermal and Magnetic properties of Strontium substituted Barium Hexaferrite Synthesized via co-precipitation Method, International Journal of ChemTech Research 8 (2015) 404-410.

[26] Prasad, N.K. Naulakha, A. Jha, N. Meena, S.S. Bahadur, D. Prakash, O. Mandal, R.K. Magnetic and electric properties of nanoparticles of Ni-substituted ferrites synthesized using a microwave refluxing process, Int. J.Mater.Res.104 (2012) 680-685.

[27] Punitha, J.S., Raji, R.K., Kumar, K.S. et al. Investigating the impact of Gd3+ ion substitution in Sr2FeTiO6: insights into magnetic, electrical, and structural properties. Appl. Phys. A 130, 825 (2024).

[28] Trukhanov, A. Zhao, X. Kostishin, V. Tishkevich, D. Trukhanova, E. Almessiere, M. Baykal, A. Slimani, Y. Sayyed, M. Rotkovich, A. et al. Evolution of the structural parameters and magnetic characteristics in "ferrite/polymer" nanocomposites J. Alloys Compounds, 986 (2024), p. 174048.

[29] Ishaque, M. Islam, M.U. Azhar Khan, M. Rahman, I.Z. Genson A. Hampshire, S. Microstructure and Microwave Absorption Properties of Y-Substituted Ni-Zn Ferrites, Physica B. 405 (2010) 1532-1540.

[30] M. Dhilip, R. K. Raji, K. S. Kumar and V. Anbarasu, "Exploring Photoluminescence Properties of Fe-Doped Dy2O3 for Enhanced Optoelectronics device Performance," 2025 IEEE 7th International Conference on Emerging Electronics (ICEE), Bengaluru, India, 2025, pp. 1-3, doi: 10.1109/ICEE67165.2025.11409749.

[31] Tholkappiyan, R. Vishista, K. N-N-methylene bis acrylamide: A novel fuel for combustion synthesis of zinc ferrite nanoparticles and studied by X-Ray photoelectron spectroscopy, International Journal of ChemTech Research 6 (2014) 2834-2842.

[32] R.K. Raji, V. Kurapati, T. Ramachandran, et al., Tweaking the red emission, magneto, and dielectrical properties of perovskite type-LaFeO3 in the presence of Co substitution, J. Mater. Sci. Mater. Electron. 31 (2020) 7998–8014, https://doi. org/10.1007/s10854-020-03340-8.

[33] Preparation of magnetic spinel ferrite core/shell nanoparticles: soft ferrites on hard ferrites and vice versa Solid State Sci., 8 (9) (2006), p. 1015-1022.

[34] Dhilip, M., Saravana Kumar, K., Ramesh Kumar, R. et al. Intrinsic Magnetic and Ferroelectric Behaviour of Non-magnetic Al3+ Ion Substituted Dysprosium Iron Garnet Compounds. J. Electron. Mater. 48, 8243–8253 (2019).

[35] R.K. Raji, T. Ramachandran, M. Muralidharan, et al., Twitching the inherent properties: the impact of transition metal Mn-doped on LaFeO3-based perovskite materials, J. Mater. Sci. Mater. Electron. 32 (2021) 25528–25544, https://doi. org/10.1007/s10854-021-07018-7.

[36] Asghar, G. Anis-ur-Rehman, M. Structural, dielectric and magnetic properties of Cr–Zn doped strontium hexa-ferrites for high

frequency applications, J. Alloys Compound 526 (2012) 85-90.

[37] Iqbal, M.J. Ashiq, M.N. Physical and electrical properties of Zr–Cu substituted strontium hexaferrite nanoparticles synthesized by co precipitation method, Chem. Eng. J. 136 (2008) 383.

[38] 16. S. Kartik, Dhanasekaran Prakash, R. Ramesh Kumar, V. Ramkumar, K. Vishista, Hanumant Singh Rathore, R. C. Panda & T. Senthilvelan, Betel leaf-derived carbon nano-sphere/renewable resourced polyurethane coatings for high-performance applications. Polym. Bull. 78, 3527–3541 (2021).

[39] R.K. Raji, T. Ramachandran, M. Muralidharan, et al., Dual-phase formation in LaFeO3 upon doping of rare-earth Dy3+: struct–opto–dielectric–magnetic characteristics, J. Mater. Sci. Mater. Electron. 33 (2022) 10626–10644, https://doi.org/10.1007/s10854-022-08047-6.

[40] Hakola, A. Heczko, O. Jaakkola, A. Kajava, T. Ullakko, K. Pulsed laser deposition of NiMnGa thin films on silicon, Applied physics A 79 (2004) 1505-1508.

[41] R. Suriakarthick, M. Senthil Pandian, P. Ramasamy, Ramesh Kumar Raji, M. Muralidharan, C.K Amaljith, Suresh Sagadevan, Solvothermal synthesis, structural and transport properties of polycrystalline copper tin selenide for thermoelectric applications, Inorg. Chem. Commun., Vol 140, 2022, 109491, 1387-7003,

[42] Pramanik, N.C. Fujii, T. Nakanishi, M. Takada, J. Seok, S.I. The effect of heat treatment temperature on the microstructure and magnetic properties of Ba2Co2Fe12O22 (Co2Y) prepared by sol–gel method, MaterLett. 60 (2006) 2718-2722.

[43] R.K. Raji, T. Ramachandran, F. Hamed, S. S., Tailoring multiferroic characteristics in LaFeO3 nanocrystals via rare-earth Pr3+ doping, Adv. Condens. Matter Phys. 2023 (1) (2022) 7369790.

[44] Zhong, W. Ding, W. Zhang, N. Hong, J. Yan, O. Du, Y. Key step in synthesis of ultrafine BaFe12O19 by sol-gel technique, J. Magn Mater 168 (1997) 196-202.

[45] Jun Li Zhang Structural and Magnetic Behavior of Chromium Doped Ba0.5Sr0.5Fe12O19 Nanoparticles Synthesized by Chemical Co-Precipitation Technique, Applied Mechanics and Materials 274 (2013) 406-410.

[46] Kim, S.G. Wang, W.N. Iwaki, T. Yabuki, A. Okuyama, K. Low-temperature crystallization of barium ferrite nanoparticles by a sodium citrate-aided synthetic process, J. Phys. Chem.C 111 (2007) 10175–10180.

[47] Maensiri, S. Masingboon, C. Banjong, C. Seraphin, S. A simple route to synthesize nickel ferrite (NiFe2O4) nanoparticles using egg white, Scr. Mater. 56 (2007) 797–800.

[48] Raji, R.K.; Ramachandran, T.; Dhilip, M.; Aravindan, V.; Punitha, J.S.; Hamed, F. Integrating Experimental and Computational Insights: A Dual Approach to Ba2CoWO6 Double Perovskites. Ceramics, (2024), 7, 2006-2023.

[49] Raji, R.K., Ramachandran, T., Punitha, J.S. et al. Structural and functional analysis of Eu3+-doped Sr2FeTiO6 perovskites: insights into electrical and magnetic characteristics. J Mater Sci: Mater Electron 36, 120 (2025).

[50] Shepherd, P. Mallick, K. Green, R. Magnetic and structural properties of M-type barium hexaferrite prepared by coprecipitation, Journal of Magnetism and Magnetic Materials 311 (2007) 683–692.

[51] Mosleh, Z. Kamelin, P. Ranjbar, M. Salamati, H. Effect of annealing temperature on structural and magnetic properties of BaFe12O19 hexaferrite nanoparticles, Ceramics International 40 (2014) 7279–7284.

[52] D. Venkatesh, V. Kanchana, S. Vasanthan, A. Kistan, P. Rajeswaran, K. Arunkumar, P.S. Karthik Design and fabrication of magnetically recoverable sno2/cofe2o4 nanocomposite for enhanced visible light-driven wastewater treatment Inorganic Chem. Commun. (2024), p. 112657.

[53] M. Dhilip, S. Rameshkumar, R.K. Raji, T. Ramachandran, J.S. Punitha, F. Regan Maria Sundar Raj, K.S. Kumar, V. Anbarasu, N. Sekar, R. Chinnathambi, A. A. Ghfar, Combined experimental and theoretical investigation on the structural, electronic, magnetic and optical properties of Pr2CoFeO6 double perovskite, Mater.Today Commun. 38 (2024) 108120.

[54] Jelli,, M. Vidyasagar, T. CV, K.R. Naidu, K.C.B 'Narrow band gap and high saturation magnetization in y-doped nico ferrites J. Superconduct. Novel Magnetism', 37 (1) (2024), p. 205-215.

[55] Raji, Ramesh Kumar, Ramachandran, Tholkappiyan, Muralidharan, M., Suriakarthick, R., Dhilip, Muthu, Hamed, Fathalla and Kurapati, Vishista. "Conventional synthesis of perovskite structured LaTixFe1-xO3: A comprehensive evaluation on phase formation, opto-magnetic, and dielectric properties" International Journal of Materials Research, vol. 112, no. 9, 2021, pp. 753-765.

[56] Sharma, P. Rocha, R.A. De Medeiros, S.N. PaesanoJr, A. Structural and magnetic studies on barium hexaferrites prepared by mechanical alloying and conventional route, J. Alloys Comp 443 (2007) 37–42.

[57] Lechevallier, L. Le Breton, J.M. Wang, J.F. Harris, I.R. Structural analysis of hydrothermally synthesized Sr1−xSmxFe12O19 hexagonal ferrites, J. Magn. Magn.Mater. 269 (2004)192-196.

[58] Sandaranarayanan, VK, & Khan, D.C. 'Mechanism of the Formation of Nanoscale M-Type Barium Hexaferrite in the Citrate Precursor Method', Journal of Magnetism and Magnetic Materials, 153 (1996), 337-346.

[59] Schloemann, E 2000, 'Advances in ferrite microwave materials and devices', J. Magn. Magn. Mater. 209 (2000), 15-20.

[60] Berdous, D. Kenfoud, H. Trari, M. Physico-chemical properties of the spinel cafe2o4 synthesized by sol–gel route: application to drimarene green x-3g photo degradation, React. Kinetics, Mechan.Catal. 136 (1) (2023) 507–522.

[61] R. Kameshwaran, A. Raja, R. Ramesh Kumar, D. Joseph Daniel, D.O. Annalakshmi, K. Aravinth, P. Balaji Bhargav, P. Ramasamy, Synthesis, structure and luminescence properties of bifunctional KCaF3 phosphor influenced by incorporating Eu3+ ions for solid state lighting and TL dosimetry applications, Applied Radiation and Isotopes, 191, 2023, 110520, 0969-8043,

[62] Umashankara Raja, R. Manjunatha, R. Vidya, H.C. Krishnakanth,Y.S. Munirathnam, E. Rajashekara, R. Manjunatha, K.M. 'The structural, magnetic and electrical properties of chromium doped calcium ferrite nanoparticles' Chemical Physics Impact 9 (2024) 100710.